Progress In Electromagnetics Research B, Vol. 103, 75–99, 2023

Sensorless Control of Interior Permanent Magnet Synchronous Motor with Triangular Transform Current Self-Demodulation in the Estimating *d-q* Axis

Dingdou Wen[1], Xincheng Zhu[1], Zhun Cheng[2, *], Yanqin Zhang[1], and Wenting Zhang[1]

Abstract—To address the issues of complex current demodulation, large rotor position estimation error, and position estimation error varying with speed in the high-frequency (HF) rotating voltage injection (HRVI) method for interior permanent magnet synchronous motor (IPMSM), a sensorless control of IPMSM with triangular transform (TT) current self-demodulation in the estimating *d-q* axis is proposed. Firstly, the HF currents estimated on the *d* and *q* axes are multiplied, and the resulting signal is constructed through TT to achieve phase shift compensation of positive and negative sequence HF currents. At the same time, a position error signal is constructed. Then, a low-pass filter is used to extract the position error signal and achieve self-demodulation of the current. The experimental results show that this method reduces the average position error by 15.0% under steady-state conditions and reduces the fluctuation range of position error by 17.6% under full load conditions.

1. INTRODUCTION

Interior permanent magnet synchronous motor (IPMSM) is widely used in various industrial fields such as electric vehicles and aerospace due to its simple structure, high efficiency, high power density, and high torque density [1–3]. To achieve high performance vector control for IPMSM, obtaining high precision speed information and rotor position information is the key to control. However, using mechanical position sensors to obtain rotor information brings problems such as poor reliability, high cost, and system complexity [4, 5]. Therefore, the sensorless control of IPMSM has become a research hotspot [6, 7].

In practical engineering applications, the speed operating conditions of IPMSM are usually divided into two cases: zero-low speed and medium-high speed. The model method is usually used for medium and high-speed conditions, and this method mainly uses back electromotive force (EMF) to estimate the rotor position [8, 9], which has good performance. However, at zero and low speed, EMF is very small or even close to zero, which is difficult to detect and is not suitable for zero and low speed situations [10, 11]. The high-frequency (HF) injection method is usually used at zero and low speeds. This method obtains rotor position information accurately by applying HF excitation signals and utilizing motor saliency effect. The HF injection method can be divided into three categories: HF rotating signal injection method [12], HF pulsating signal injection method [13], and HF square wave signal injection method [14]. The implementation process of HF pulsating signal injection method is relatively simple, but there are problems such as long convergence time and insufficient stability [15, 16]. The HF square wave signal injection method omits the low pass filter (LPF) and has good dynamic performance, but there

Received 4 July 2023, Accepted 18 October 2023, Scheduled 4 November 2023

* Corresponding author: Zhun Cheng (120277982@qq.com).

[1] Hunan University of Technology, Zhuzhou 412007, China. [2] Hunan Railway Professional Technology College, Zhuzhou 412001, China.

are noise issues and HF torque ripple issues [17]. Compared to the two methods, HF rotational signal injection (HRVI) is widely used for sensorless control of IPMSM due to its low parameter sensitivity, strong stability, and ease of engineering implementation [18].

The HRVI method mainly consists of three parts: HF signal injection, current demodulation, and rotor position estimation. HF signal injection is the injection of rotating HF voltage signals in the α-β axis. Current demodulation is used to obtain rotor position error signals. The rotor position estimation is achieved by observing the demodulated rotor signal through a position observer. So, the current demodulation method to a certain extent determines the accuracy of the estimated position signal and the complexity of the rotating HF voltage injection method. The conventional HRVI method uses a synchronous frame high pass filter (SFHF) to demodulate the current. This method requires the use of demodulated signals to complete the demodulation. The current demodulation process is complex, and due to the phase shift of the HF current, the estimation error of the rotor position will be large. With the improvement of digital chip processing performance, model predictive control (MPC) has also been applied in sensorless control. In [19], a sensorless control method is proposed which combines finite position set phase-locked loop and MPC, avoiding the use of proportional integral (PI) controllers and further improving the robustness of the system. However, the positional error is influenced by the accuracy of the algorithm and requires a significant amount of computation. In [20], virtual vector and duty cycle control are introduced to predict significant steady-state fluctuations and computational burden in current control with limited control set models. This method reduces the complexity of the control system and improves the steady-state performance of MPC. However, the synthesis of virtual vectors is limited by the synthesis method, and further analysis is needed. field oriented control (FOC) still has certain advantages in engineering applications. In [21], based on the current of the SFHF method, a strategy for extracting error angles to compensate for negative sequence high-frequency current is proposed, reducing position errors. However, this method requires the use of two demodulation signals to extract error angles and separate positive and negative sequence currents, resulting in a complex demodulation process. In [22], the amplitude of three-phase current is demodulated by the recursive discrete Fourier transform method, which suppresses the system delay and the phase shift caused by the filter. However, this method increases the computational complexity of the system and makes the demodulation process more complex. In [23], a demodulation method is proposed in the estimating d-q axis, which eliminates the errors caused by system delay and band pass filter (BPF) phase shift at zero and low speeds. However, in the current demodulation process, two demodulation signals are still needed to achieve the separation of positive and negative sequence HF signals and the extraction of position signals. The current demodulation process is still relatively complex. In [24], an improved self-adjusting frame amplitude convergence (SFAC) current demodulation method is proposed, which extends the speed applicability of the SFAC method from zero speed zone to non-zero speed zone, simplifying the current demodulation process to some extent, but additional demodulation signals need to be constructed to complete the demodulation. In [25], an estimated position feedback current demodulation method is proposed to eliminate the effect of rotational speed on position error, but it still needs to construct two demodulation signals to complete the positive and negative sequence HF current separation and position error compensation. In [26], the HF orthogonal square wave signal is injected into the a-b axis, and the periodicity of the Trigonometric functions is used to realize current demodulation. This method omits LPF and improves the dynamic performance of the system. However, the separation process of positive and negative sequence HF currents is still complex and requires a large amount of calculation. In addition, this method is essentially HF square wave injection method, which has problems such as noise. In [27], HF response current self-demodulation method is proposed, which does not require the construction of auxiliary demodulation signals to achieve current self-demodulation and simplify the complexity of the system. However, it still requires the separation of positive and negative sequence HF currents and does not consider the impact of speed on position estimation error.

The demodulation method mentioned above reduces the rotor position error to a certain extent, but while reducing the error, it also makes the current demodulation process more complicated. This paper improves the demodulation process of the rotating HF injection method, which is simpler than the methods in [25] and [27]. The main contributions of this paper are as follows:

(i) A current demodulation method has been proposed, which can construct the required position error signal through TT with just one multiplication operation. Compared with traditional methods,

this method has a simple process and does not rely on demodulated signals.

(ii) By utilizing the equal and opposite angular frequencies of positive and negative sequence HF currents on the estimated d-q axis, phase shift compensation is achieved, reducing the influence of velocity on position error.

(iii) The proposed method can reduce the phase shift caused by LPF during the current demodulation process.

The rest of the paper is organized as follows. Section 2 introduces the conventional HF rotating injection method. Section 3 analyzes the phase shift produced by non-ideal factors on HF currents. Section 4 describes in detail the principle and implementation process of the TT current self-demodulation method for α-β axis and the estimating d-q axis. Section 5 provides experimental results and analysis. Finally, Section 6 gives the conclusions.

2. CONVENTIONAL HRVI METHOD

2.1. The HF Excitation Voltage Equation of IPMSM

The fundamental voltage equation of IPMSM is expressed as:

$$\begin{bmatrix} u_d \\ u_q \end{bmatrix} = \begin{bmatrix} R & -\omega_e L_q \\ \omega_e L_d & R \end{bmatrix} \begin{bmatrix} i_d \\ i_q \end{bmatrix} + \begin{bmatrix} L_d & 0 \\ 0 & L_q \end{bmatrix} \frac{d}{dt} \begin{bmatrix} i_d \\ i_q \end{bmatrix} + \begin{bmatrix} 0 \\ \omega_e \psi_f \end{bmatrix} \tag{1}$$

where u_d and u_q are the d and q-axis components of the stator voltage. i_d and i_q are the d and q-axis components of the stator current. L_d and L_q are the d and q-axis components of the inductor. R is the stator resistance. ω_e is the electric angular velocity, and ψ_f represents the permanent magnet flux linkage.

When the HF excitation signal is injected into the motor, its frequency is far higher than the fundamental frequency of the motor. At the zero speed or low speed, the self-inductance reactance in the winding is much larger than the stator resistance R, and the influence of resistance s ignored. The cross-coupling terms $\omega_e L_d$, $-\omega_e L_d$ and induced electromotive force $\omega_e \psi_f$ are also ignored [18]. The voltage equation of IPMSM under HF excitation is simplified as:

$$\begin{bmatrix} u_{dh} \\ u_{qh} \end{bmatrix} = \begin{bmatrix} L_{dh} & 0 \\ 0 & L_{qh} \end{bmatrix} \frac{d}{dt} \begin{bmatrix} i_{dh} \\ i_{qh} \end{bmatrix} \tag{2}$$

where u_{dh}, $u_{qh} i_{dh}$, i_{qh}, L_{dh}, and L_{qh} represent the HF voltage, HF current, and HF inductance of the d-q axes, respectively.

2.2. High Frequency Current Response of IPMSM

The principle of HF rotating injection is shown in Fig. 1, and the positional relationship of each axis is shown in Fig. 2. Firstly, HF voltage excitation is injected into the α-β axis to generate a corresponding HF current in the motor stator. Then, the detected current signal is subjected to specific signal processing. Finally, the position information of the rotor is extracted from the phase of the HF current. The process is summarized as three steps: HF injection, current demodulation, and position observation [24, 25]. The actual injected voltage is expressed as follows:

$$u_{\alpha\beta h} = \begin{bmatrix} u_{\alpha h} \\ u_{\beta h} \end{bmatrix} = \begin{bmatrix} V_h \cos \omega_h t \\ V_h \sin \omega_h t \end{bmatrix} = V_h e^{j\omega_h t} \tag{3}$$

where $u_{\alpha h}$ and $u_{\beta h}$ represent HF voltage signals injected into the α axis and β axis. V_h and ω_h represent the amplitude and angular frequency of the injected HF voltage signal.

After transforming (3) into the d-q axis through Park and substituting it into (2), the HF current response in the d-q axis is obtained as follows:

$$\mathrm{i}_{dqh} = I_p e^{j\left(\omega_h t - \theta_e - \frac{\pi}{2}\right)} + I_n e^{j\left(-\omega_h t + \theta_e + \frac{\pi}{2}\right)} \tag{4}$$

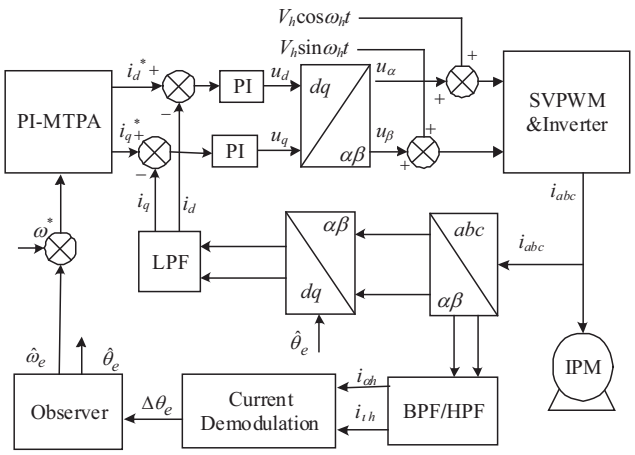

Figure 1. The schematic diagram of HF rotating injection.

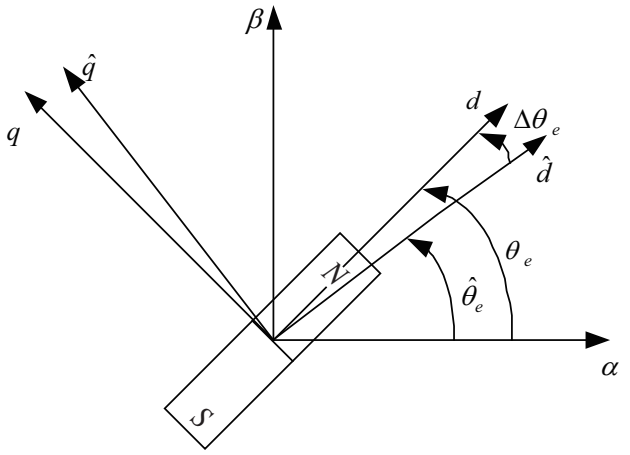

Figure 2. The positional relationship of each axis.

where θ_e is the actual position of the rotor, and I_p and I_n represent the amplitude of the positive sequence and negative sequence HF current components, respectively. The expressions are as follows:

$$I_p = \frac{V_h}{\omega_h L_{dh} L_{qh}} \cdot \frac{L_{dh} + L_{qh}}{2} \tag{5}$$

$$I_n = \frac{V_h}{\omega_h L_{dh} L_{qh}} \cdot \frac{L_{dh} - L_{qh}}{2} \tag{6}$$

Transforming (4) to the α-β axis by inverse Park, the HF current expression is:

$$\begin{bmatrix} i_{\alpha h} \\ i_{\beta h} \end{bmatrix} = i_{\alpha\beta h} = i_{dqh} e^{j\theta_e} = I_p e^{j\left(\omega_h t - \frac{\pi}{2}\right)} + I_n e^{j\left(-\omega_h t + 2\theta_e + \frac{\pi}{2}\right)} \tag{7}$$

where $i_{\alpha h}$ and $i_{\beta h}$ represent the HF response current of the α axis and β axis, respectively.

From (7), the positive sequence HF current component does not contain rotor position related information, and only the phase of the negative sequence HF current component contains rotor position information. Therefore, the rotor position information is obtained by extracting the negative sequence component from the HF current.

Transforming (7) by coordinates, the estimated HF current in the d-q axis is obtained as:

$$\hat{i}_{dqh} = I_p e^{j\left(\omega_h t - \hat{\theta}_e - \frac{\pi}{2}\right)} + I_n e^{j\left(-\omega_h t + 2\theta_e - \hat{\theta}_e + \frac{\pi}{2}\right)} \tag{8}$$

where $\hat{\theta}_e$ is the estimated position of the rotor.

From (8), if the phases in the positive and negative sequence HF current components are added, the position error signal is constructed directly. Therefore, the rotor position error signal is directly constructed to extract the rotor position signal.

2.3. Conventional Current Demodulation and Position Estimation Methods

To extract the rotor position information from the negative sequence HF current, it is necessary to demodulate the HF current. Current demodulation includes two processes: separating the positive and negative sequence HF currents and extracting the rotor position signal. The conventional HRVI method uses the SFHF demodulation method. The SFHF demodulation method and position estimation implementation are shown in Fig. 3.

The SFHF method transforms the HF current into a reference coordinate system that rotates synchronously with the injected high-frequency voltage through coordinate transformation, where the positive sequence HF current component is regarded as a constant. By filtering it out through a high-pass filter (HPF), the negative sequence HF current is obtained. After coordinate transformation, the

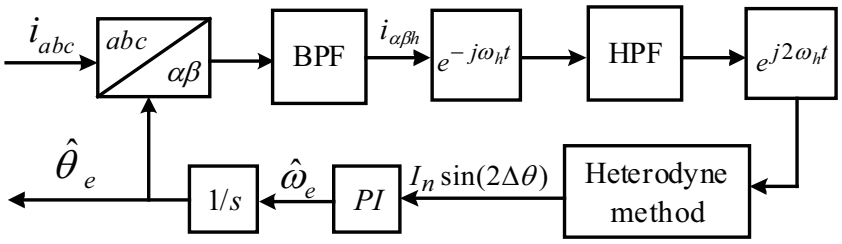

Figure 3. Schematic diagram of SFHF current demodulation.

negative sequence HF current is transformed back into the α-β axis, achieving the separation of positive and negative sequence HF currents.

After separating the positive and negative sequence HF currents, the heterodyne method is used to construct the rotor position error and extract the actual rotor position signal. The mathematical implementation of the heterodyne method is shown in (9), and the schematic diagram of the implementation is shown in Fig. 4.

$$f(\Delta\theta) = i_{ah}^n \cos(2\hat{\theta}_e - \omega_h t) + i_{\beta h}^n \sin(2\hat{\theta}_e - \omega_h t) = I_n \sin(2\theta_e - 2\hat{\theta}_e) \approx 2I_n \Delta\theta \tag{9}$$

where $\Delta\theta$ is the positional error. When $\theta_e - \hat{\theta}_e$ tends towards 0, there is $\sin(2\theta_e - 2\hat{\theta}_e) = 2\Delta\theta$.

As can be seen from Fig. 4, after constructing the error signal, the PI regulator adjusts the error signal to zero to obtain the estimated electrical angular velocity and then integrates the estimated electrical angular velocity to obtain the estimated rotor position. To improve conventional method, this paper summarizes the shortcomings of conventional methods, as shown in Table 1.

Table 1. Shortcomings of conventional methods.

Method	Demodulation process	Demodulated signal	Speed correlation	Position error
Conventional method	Complex	Yes	Yes	Large

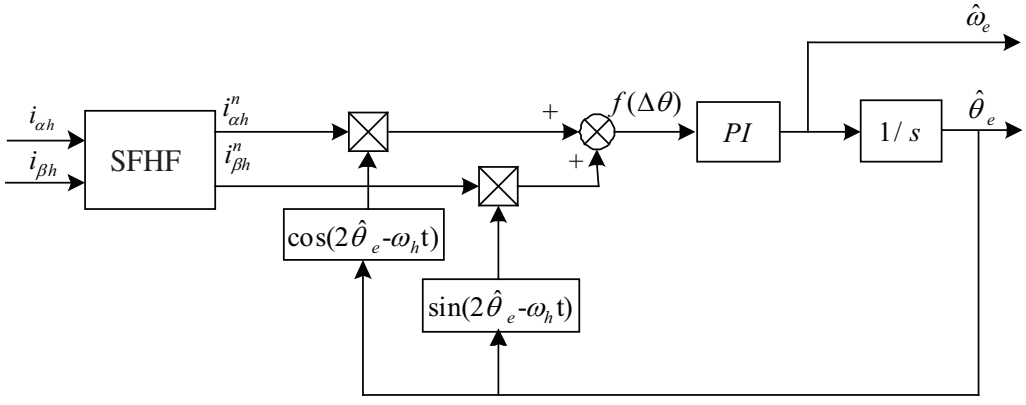

Figure 4. Schematic diagram of heterodyne method implementation.

3. ANALYSIS OF PHASE SHIFT CAUSED BY NON-IDEAL FACTORS ON HF CURRENT

3.1. Phase Shift Caused by System Delay

In digital control systems, it is inevitable to introduce system delay, which has a relatively small period relative to the fundamental current and is ignored in the fundamental current [27]. But in HF current, due to the small period of HF current, the two are similar in size, and the system delay is about 1.5 times of the HF current period [21]. This delay cannot be ignored in HF signals. The phase shift caused by system delay in HF current is expressed as:

$$\varphi_{\mathrm{d}} = \omega_i t_{\mathrm{d}} \tag{10}$$

where φ_{d} is the phase shift generated by the system delay. ω_i is the HF electrical angular velocity when the speed is stable. t_{d} is the system delay.

φ_{d} is regarded as an odd function with ω_i as the unknown number; therefore, it has the odd function characteristic, namely: $f(-x) + f(x) = 0$. This characteristic is used to cancel the phase shift of positive and negative sequence HF currents. The phase shifts caused by the system delay on positive and negative sequence HF currents are represented by $\varphi_{\mathrm{p}}^{dely}$ and φ_n^{dely}.

3.2. Phase Shift Generated by the Filter

As shown in Fig. 1, it is necessary to use BPF or HPF to process the signals, when extracting HF signals and separating positive and negative sequence HF currents. In addition, in the current demodulation process, it is usually necessary to use LPF to separate positive and negative sequence HF currents. When the HF current signal passes through the filter, the HF signal will generate phase shift.

The paper takes BPF, HPF, and LPF as examples to analyse the relationship between current frequency and filter phase shift. The frequency of HF injection signals is usually 0.5–2 kHz [28]. The HF injection signal selected is 500 Hz. Consider that when the passband of the filter is low, the filtering effect is good, but the angle lag is large, and the dynamic performance is poor. If the filtering passband is large, the angle lag is small, and the dynamic performance is good, but the filtering effect is poor. There are many harmonics in the extracted signal based on simulation experiments and analysis, and the cut-off frequency of the filter has been determined. We have set the passband range of BPF to 450–500 Hz, the cutoff frequency of HPF to 200 Hz, and the cutoff frequency of LPF to 100 Hz [21, 23, 29]. The transfer functions of BPF, HPF, and LPF are as follows:

$$H_1(s) = \frac{628s}{s^2 + 628s + 9859600} \tag{11}$$

$$H_2(s) = \frac{s}{s + 1256} \tag{12}$$

$$H_3(s) = \frac{628}{s + 628} \tag{13}$$

According to (11), (12), and (13), the phase frequency response diagrams of BPF, HPF, and LPF are obtained, as shown in Fig. 5.

As shown in Fig. 5, when the input signal frequency is 0.5 kHz, BPF and HPF will generate phase shifts of approximately 2.28° and 20°, respectively, denoted as φ_p^{BPF} and φ_p^{HPF}. When the input frequency signal is −0.5 kHz, BPF and HPF will generate phase shifts of approximately −2.28° and −20°, denoted as φ_n^{BPF} and φ_n^{HPF}. Therefore, the phase shifts φ_{BPF} and φ_{HPF} generated by BPF and HPF on HF currents have odd function characteristics on the frequency of HF currents. When the input signal frequency is ±20 Hz, LPF will generate a phase shift of approximately ±2.30°, denoted as φ_p^{LPF} and φ_n^{LPF}. Let φ_{LPF} represent the phase shift generated by LPF on HF currents. When the input frequency approaches 0, the phase shift generated by LPF is close to 0, so this characteristic can be used to eliminate the phase shift generated by LPF.

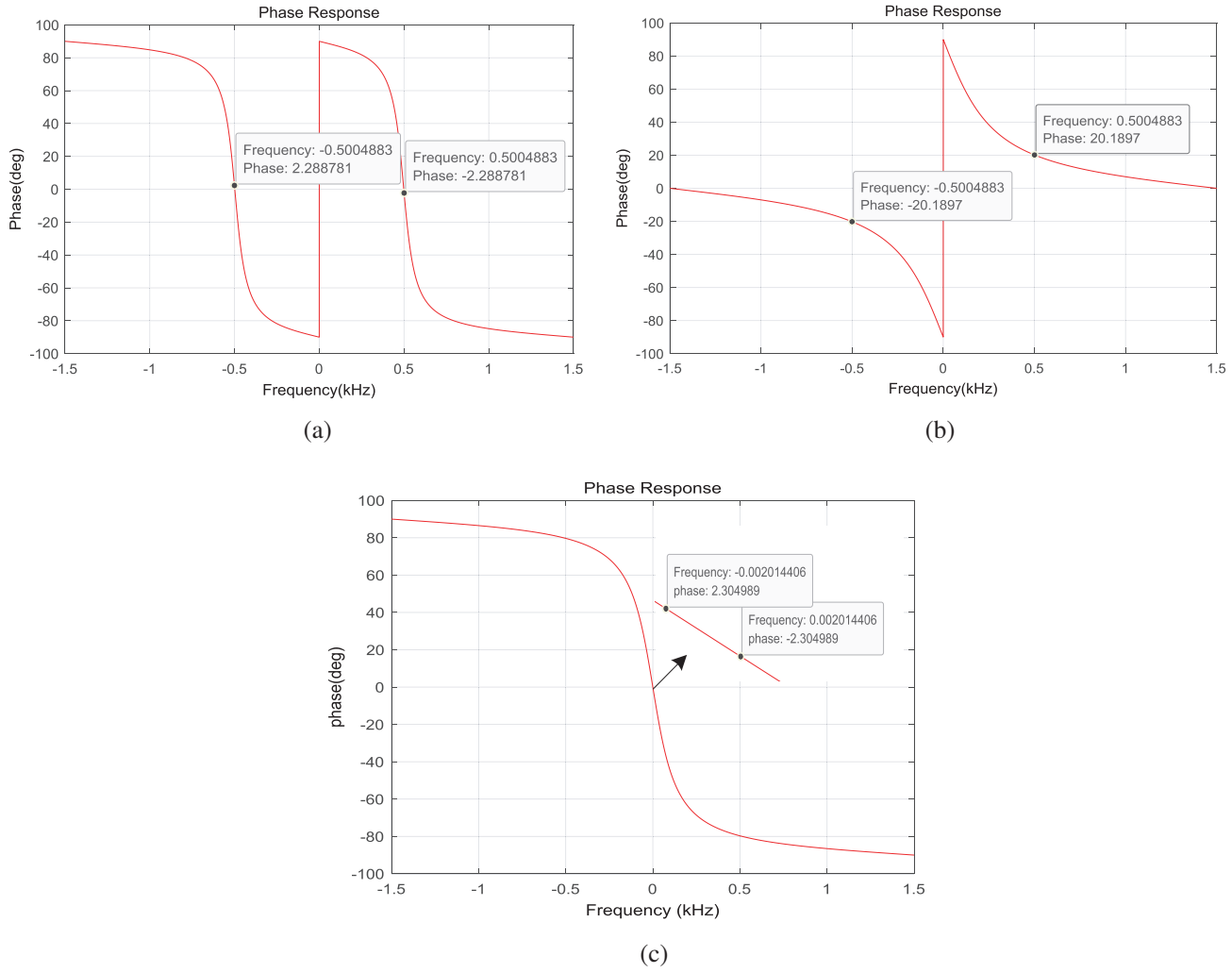

Figure 5. Filter phase frequency response diagram. (a) BPF. (b) HPF. (c) LPF.

3.3. Phase Shift Generated by PI Regulator

In the HRVI, the block diagram of the PMSM vector controlled Current loop is simplified as shown in Fig. 6, and the transfer function between the injected HF voltage and current are obtained as follows:

$$G_{ui}(s) = \frac{s}{Ls^2 + (k_p + R_s)\mathrm{s} + k_i} \tag{14}$$

where L and R_s are the motor and stator resistances. k_p and k_i are the proportional integral regulator coefficients of the Current loop.

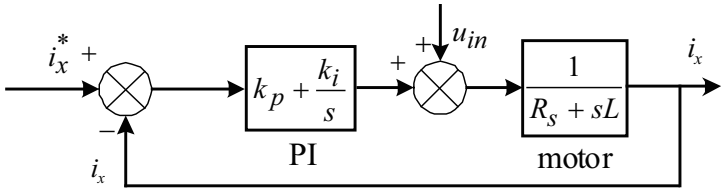

Figure 6. Block diagram of transfer function of Current loop.

By incorporating $s = j\omega$ into (14), the frequency response expression is obtained:

$$G_{\mathrm{ui}}(j\omega) = \frac{j\omega}{L(j\omega)^2 + (k_p + p_s)j\omega + k_i} \tag{15}$$

$$\angle G_{\mathrm{ui}}(j\omega) = \arctan\frac{(k_p + R_s)\omega}{L\omega^2 - k_i} - 90^\circ = \varphi_{pi}(\omega) - 90^\circ \tag{16}$$

According to (16), the phase of the HF current no longer lags behind the HF voltage by 90°. When HF current passes through current loop PI regulator, phase shift φ_{pi} will occur. The phase shift generated by current loop PI regulator for positive and negative sequence HF current is recorded as φ_p^{pi} and φ_n^{pi}, respectively.

In summary, the phase shifts φ_p^{sum} and φ_n^{sum} caused by non-ideal factors on the positive and negative sequences of HF currents are expressed as:

$$\begin{cases} \varphi_p^{sum} = \varphi_{\mathrm{p}}^{dely} + \varphi_p^{filter} + \varphi_p^{pi} \\ \varphi_n^{sum} = \varphi_n^{dely} + \varphi_n^{filter} + \varphi_n^{pi} \end{cases} \tag{17}$$

where φ_p^{filter} and φ_n^{filter} represent the phase shifts generated by BPF or HPF on positive and negative sequence HF currents, respectively.

Considering the phase shift, the HF currents in the α-β axis and the estimating d-q axis are expressed as:

$$i_{\alpha\beta h} = I_p e^{j\left(\omega_h t + \varphi_p^{sum} - \frac{\pi}{2}\right)} + I_n e^{j\left(-\omega_h t + 2\theta_e + \varphi_n^{sum} + \frac{\pi}{2}\right)} \tag{18}$$

$$\hat{i}_{dqh} = I_p e^{j\left(\omega_h t - \hat{\theta}_e + \varphi_p^{sum} - \frac{\pi}{2}\right)} + I_n e^{j\left(-\omega_h t + 2\theta_e - \hat{\theta}_e + \varphi_n^{sum} + \frac{\pi}{2}\right)} \tag{19}$$

From (18) and (19), both the positive and negative sequence HF currents contain a large amount of phase shifts. To improve the accuracy of position estimation, it is necessary to eliminate the impact of these phase shifts on the rotor position error.

4. IMPROVED HRVI METHOD

4.1. Frequency Analysis of Positive and Negative Sequence HF Currents in the α-β Axis and the Estimating d-q Axis

The rotor position signal is described as:

$$\theta_e = \int \omega_e dt \tag{20}$$

When the motor speed is stable, the estimated rotor position and the actual rotor position are represented as $\hat{\theta}_e = \hat{\omega}_e t$ and $\theta_e = \omega_e t$. Currently, $\hat{\omega}_e$ is very close to ω_e, $\hat{\omega}_e \approx \omega_e$. Equations (18) and (19) are rewritten as follows:

$$\mathrm{i}_{\alpha\beta h} = I_p e^{j\left(\omega_h t + \varphi_p^{sum} - \frac{\pi}{2}\right)} + I_n e^{j\left(-\omega_h t + 2\omega_e t + \varphi_n^{sum} + \frac{\pi}{2}\right)} \tag{21}$$

$$\hat{i}_{dqh} = I_p e^{j\left((\omega_h - \hat{\omega}_e)t + \varphi_p^{sum} - \frac{\pi}{2}\right)} + I_n e^{j\left(-(\omega_h - \hat{\omega}_e t + \varphi_n^{sum} + \frac{\pi}{2}\right)} \tag{22}$$

The frequency and phase shift relationship of positive and negative sequence HF currents under different axes is shown in Table 2.

When $\omega_e = 0$, the positive and negative sequence HF current frequencies of the α-β axis and the estimating d-q axis are equal and have opposite signs, so the sum of positive and negative sequence phase shifts is 0, $\varphi_p^{sum} + \varphi_n^{sum} = 0$.

Based on the above analysis, it is concluded that the estimating d-q axis HF current can achieve the cancellation of the phase shift of HF current caused by non-ideal factors. In addition, the influence of speed on position estimation error is eliminated, and the accuracy of rotor position estimation is improved.

Table 2. The frequency and phase shift relationship of positive and negative sequence HF currents under different axes.

Method	Current phase sequence	Frequency	$\varphi_p^{sum}+\varphi_n^{sum}$	
			$\omega_e=0$	$\omega_e\neq 0$
α-β	Positive	ω_{h}	0	$(\varphi_p^{sum}+\varphi_n^{sum})/2$
	Negative	$-\omega_{\mathrm{h}}+2\omega_{\mathrm{e}}$		
$\hat{d}$-$\hat{q}$	Positive	$\omega_{\mathrm{h}}-\omega_{\mathrm{e}}$	0	0
	Negative	$-(\omega_{\mathrm{h}}-\omega_{\mathrm{e}})$		

4.2. TT Current Self-Demodulation Method in the α-β Axis

The separation principal diagram of positive and negative sequence HF current of conventional method and other literatures is shown in Fig. 7. Conventional methods and the methods of [21, 23, 25] separate positive and negative sequence HF current signals through additional demodulation signals and then extract rotor position signals. Although method of [27] does not require the use of demodulation signals, it still requires the separation of positive and negative sequence HF currents, and the demodulation process is still relatively complex.

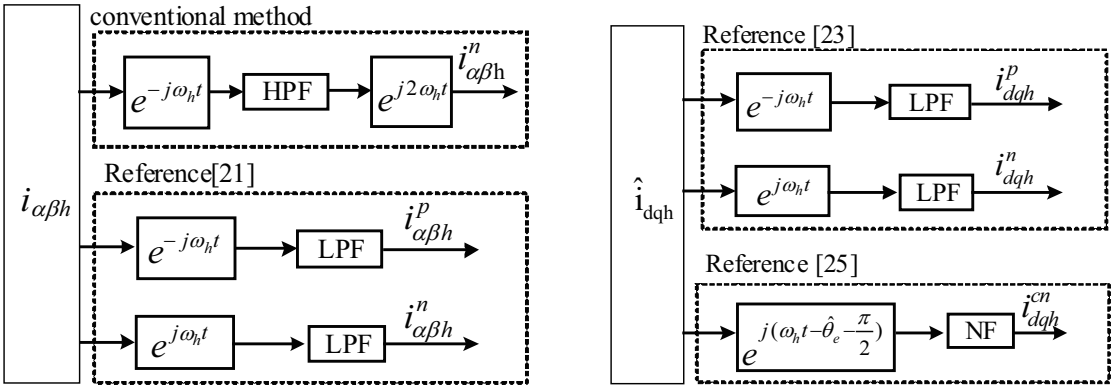

(a) conventional methods and reference [21]

(b) Reference [23] and [25]

(c) Reference [27]

Figure 7. The separation principal diagram of positive and negative sequence HF current of conventional method and other literatures.

From the perspective of practical engineering applications, if the separation of positive and negative sequences is omitted, it will reduce the complexity of the system and enhance its practicality. Therefore, this paper designs a TT current self-demodulation method in the α-β axis, which does not require the separation of positive and negative sequence signals. The rotor position signal is directly extracted through the HF currents of the α and β axes to achieve current self-demodulation. The flowchart is shown in Fig. 8.

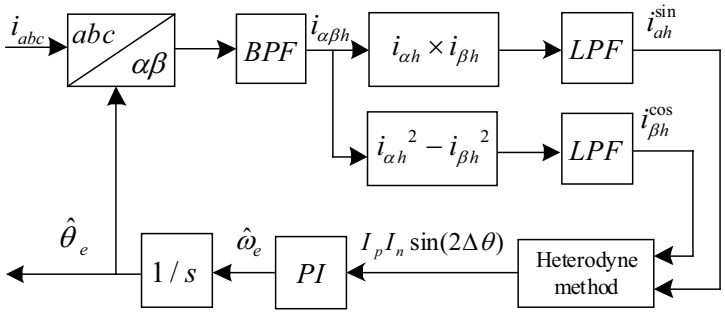

Figure 8. Schematic diagram of the TT current self-demodulation method in the α-β axis.

Rewrite (7) as:

$$\begin{bmatrix} \mathrm{i}_{\alpha h} \\ \mathrm{i}_{\beta h} \end{bmatrix} = \begin{bmatrix} I_p \cos A + I_n \cos(B) \\ I_p \sin A + I_n \sin(B) \end{bmatrix} \tag{23}$$

where A and B are:

$$\begin{cases} A = \omega_h t + -\dfrac{\pi}{2} \\ B = -\omega_h t + 2\theta_e + \dfrac{\pi}{2} \end{cases} \tag{24}$$

Multiplying $i_{\alpha h}$ and $i_{\beta h}$, $i_{\alpha h} i_{\beta h}$ is expressed as:

$$\begin{aligned} i_{\alpha h} i_{\beta h} &= I_p^2 \cos A \sin A + I_p I_n \cos A \sin B + I_p I_n \cos B \sin A + I_n^2 \cos B \sin B \\ &= \frac{I_p^2}{2} \sin 2A + \frac{I_n^2}{2} \sin 2B + I_p I_n \sin(A + B) \end{aligned} \tag{25}$$

Through LPF, $i_{ah}^{\sin}$ is expressed as:

$$i_{ah}^{\sin} = LPF(i_{\alpha h} i_{\beta h}) = I_p I_n \sin 2\theta_e \tag{26}$$

Subtracting $i_{\alpha h}^2$ and $i_{\beta h}^2$ and then using LPF, $i_{\beta h}^{\cos}$ is expressed as:

$$\begin{aligned} i_{\beta h}^{\cos} &= LPF\left\{\frac{1}{2}(i_{\alpha h}^2 - i_{\beta h}^2)\right\} \\ &= LPF\left\{\frac{1}{2}\left[I_p^2 \cos 2A + I_n^2 \cos 2B + 2 I_p I_n \cos(A + B)\right]\right\} = I_p I_n \cos 2\theta_e \end{aligned} \tag{27}$$

$$\begin{aligned} f(\Delta\theta) &= I_p I_n \sin 2\theta_e \cos 2\hat{\theta}_e + I_p I_n \cos 2\theta_e \sin 2\hat{\theta}_e \\ &= I_p I_n \sin(2\theta_e - 2\hat{\theta}_e) \approx 2 I_p I_n \Delta\theta \end{aligned} \tag{28}$$

From (26) and (27), after extracting $I_p I_n \sin 2\theta_e$ and $I_p I_n \cos 2\theta_e$, the rotor position error signal is constructed using the heterodyne method, as shown in (28). Then, the error signal is adjusted to zero through a PI regulator to obtain $\hat{\omega}_e$, and $\hat{\theta}_e$ is obtained by integrating $\hat{\omega}_e$.

After considering the phase shift of the current, rewrite (28) as follows:

$$f(\Delta\theta_{\alpha\beta}) \approx I_p I_n (2\Delta\theta_{\alpha\beta} + \varphi_p^{sum} + \varphi_n^{sum}) \tag{29}$$

At this point, $\hat{\theta}_e$ is represented as:

$$\hat{\theta}_e = \theta_e + \frac{(\varphi_p^{sum} + \varphi_n^{sum})}{2} \tag{30}$$

According to (30), $\hat{\theta}_e \neq \theta_e$, there is an error of $(\varphi_p^{sum} + \varphi_n^{sum})/2$.

Compared with the SFHF demodulation method, this method omits the process of extracting positive and negative sequence HF currents, completes self-demodulation without demodulation signals,

and reduces position estimation errors. However, this method is unable to eliminate φ_p^{LPF} and φ_n^{LPF}. When the frequencies of positive and negative sequence HF currents are not equal, φ_p^{sum} and φ_n^{sum} are unable to completely cancel out. In addition, when the speed varies, φ_p^{LPF}, φ_n^{LPF}, φ_p^{sum}, and φ_n^{sum} all change, which leads to a change in position error and makes the position error show a characteristic of changing with the speed. This characteristic is called speed correlation.

To overcome the above shortcomings, this paper proposes a TT current self-demodulation method in the estimating d-q axis.

4.3. TT Current Self-Demodulation Method in the Estimated *d-q* Axis

The TT current self-demodulation method in the α-β axis has some improvement compared to SFHF, but it incompletely eliminates the phase shift caused by non-ideal factors, and the position error varies with the speed. Therefore, this paper proposes a TT current self-demodulation method in the estimating d-q axis, as shown in Fig. 9, and the control block diagram of the proposed method is shown in Fig. 10. Compared with Fig. 8, this method omits the process of constructing $I_pI_n\cos 2\theta_e$ and uses heterodyne method to construct position error signals, further simplifying the current demodulation process.

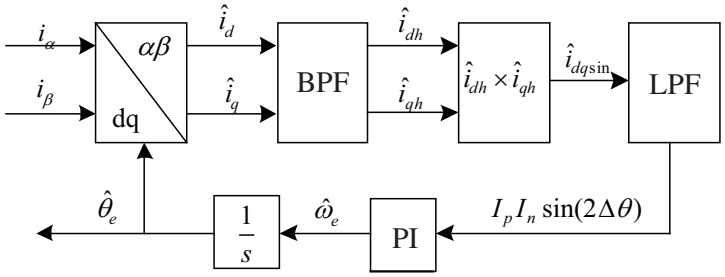

Figure 9. Schematic diagram of TT current self-demodulation method in the estimating d-q axis.

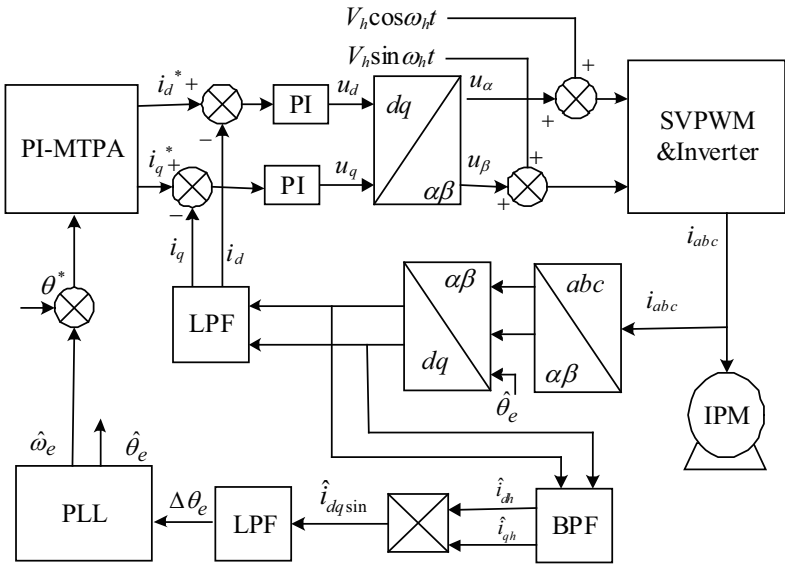

Figure 10. The control block diagram of the proposed method.

Rewrite (22) as:

$$\begin{bmatrix} \hat{i}_d \\ \hat{i}_q \end{bmatrix} = \begin{bmatrix} I_p\cos A + I_n\cos B \\ I_p\sin A + I_n\sin B \end{bmatrix} \tag{31}$$

where A and B are:

$$\begin{cases} A = \omega_h t - \hat{\theta}_e - \dfrac{\pi}{2} + \varphi_p^{sum} \\ B = -\omega_h t + 2\theta_e - \hat{\theta}_e + \dfrac{\pi}{2} + \varphi_n^{sum} \end{cases} \tag{32}$$

$$\begin{aligned} \hat{i}_{dh}\hat{i}_{qh} &= I_p^2 \cos A \sin A + I_p I_n \cos A \sin B + I_p I_n \cos B \sin A + I_n^2 \cos B \sin B \\ &= \frac{I_p^2}{2} \sin 2A + \frac{I_n^2}{2} \sin 2B + I_p I_n \sin(A+B) \end{aligned} \tag{33}$$

According to (32), $A + B = 2\theta_e - 2\hat{\theta}_e$. Multiply the estimated d-axis current by the estimated q-axis current to Equation (33). LPF is used to filter out HF signals to obtain (34).

Multiplying $\hat{i}_{dh}$ and $\hat{i}_{qh}$, $\hat{i}_{dh}\hat{i}_{qh}$ is expressed as (33), and then LPF is used to obtain (34).

$$LPF(\hat{i}_{dh}\hat{i}_{qh}) = I_p I_n \sin(2\Delta\theta) \approx 2 I_p I_n \Delta\theta \tag{34}$$

From (33), while the current is demodulated, the construction of the position error signal is completed, and the phase shift caused by non-ideal factors on the HF current is also mutually offset.

From (34), after filtering out the HF signal, the rotor position error signal is obtained. Then, through the PI regulator and integration link, $\hat{\omega}_e$ and $\hat{\theta}_e$ are obtained.

In addition, when the motor is stable, $I_p I_n \sin 2\theta_e$ is considered as a direct-current signal, and there is no phase shift when passing through LPF, thus eliminating the phase shift generated by LPF.

Compared with the TT current self-demodulation method in the α-β axis, it has the following advantages:

(i) The proposed method completes self-demodulation without demodulation signal, omits the process of separating positive and negative sequence HF currents, uses the heterodyne method to construct the rotor position error signal, and reduces computational complexity.

(ii) The proposed method completely cancels φ_p^{sum} and φ_n^{sum}, and eliminates φ_{LPF}, further reducing position error.

(iii) The proposed method eliminates the impact of speed vary on position estimation errors.

4.4. Analysis of Computational Complexity and Position Error of Different Demodulation Methods

The computational complexity of different demodulation methods is shown in Fig. 11. Conventional methods and [23] need two demodulation signals, two filters, perform 10 multiplication operations and 5 addition operations. The method of [25] needs two demodulation signals, two filters, performs 8 multiplication operations and 5 addition operations. The method of [27] performs four multiplication operations and four addition operations. The TT current self-demodulation method in the α-β axis needs a filter, performs 4 multiplication operations and 2 addition operations. The method proposed in this paper needs a filter and performs 1 multiplication operation.

From the above analysis, the method proposed in this paper has the smallest computational complexity and only needs one multiplication operation to achieve current demodulation. The computational complexity and position error comparison of different methods is shown in Table 3.

As shown in Table 3, when $\omega_e = 0$, the positive and negative sequence HF current frequencies of the TT current self-demodulation method in the α-β axis and the estimating d-q axis are equal, $\varphi_p^{sum} + \varphi_n^{sum} = 0$. However, the TT current self-demodulation method on the α-β axis is unable to eliminate φ_P^{LPF} and φ_n^{LPF}, $\Delta\theta_{\alpha\beta} = (\varphi_P^{LPF} + \varphi_n^{LPF})/2$. The position error of the TT current self-demodulation method in the estimating d-q axis is 0. When $\omega_e \neq 0$, the positive and negative sequence HF current frequencies of the TT current self-demodulation method in the α-β axis are unequal, $\Delta\theta = (\varphi_p^{sum} + \varphi_n^{sum} + \varphi_P^{LPF} + \varphi_n^{LPF})/2$. The positive and negative sequence HF current frequencies of the TT current self-demodulation method in the estimating d-q axis are still equal. The position error of the TT current self-demodulation method in the estimating d-q axis is 0, and this method eliminates speed correlation.

Table 3. The computational complexity and position error comparison of different methods

method	Computational complexity	Position Error $\Delta\theta$		
		$\omega_e = 0$	$\omega_e \neq 0$	Speed correlation
Conventional Method	Large	$(\varphi_n^{sum} + \varphi_n^{HPF})/2$	$(\varphi_n^{sum} + \varphi_n^{HPF})/2$	YES
Reference [23]	Large	0	0	NO
Reference [25]	Large	0	0	NO
Reference [27]	Medium	0	$(\varphi_p^{sum} + \varphi_n^{sum})/2$	YES
α-β	Medium	$(\varphi_p^{LPF} + \varphi_n^{LPF})/2$	$\varphi_{p+n}^{sum+LPF}/2$	YES
$\hat{d}$-$\hat{q}$	Small	0	0	NO

where $\varphi_{p+n}^{sum+LPF} = (\varphi_p^{sum} + \varphi_n^{sum} + \varphi_p^{LPF} + \varphi_n^{LPF})/2$.

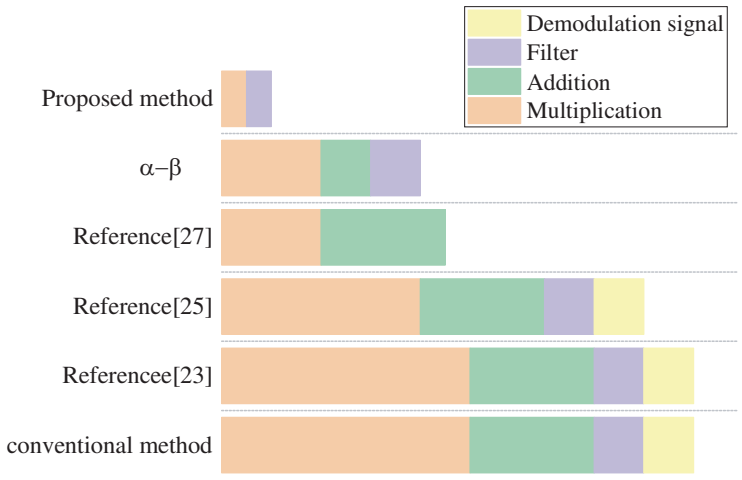

Figure 11. The computational complexity of different demodulation methods.

The conventional method does not eliminate the phase shift of the negative sequence HF current after separating the positive and sequence current signals, and has speed correlation, $\Delta\theta = (\varphi_n^{sum} + \varphi_n^{HPF})/2$.

Methods of [23] and [25] achieve phase shift cancellation of positive and negative sequence HF currents, eliminate the speed correlation of position errors, $\Delta\theta = 0$, but the computational complexity is high.

Computational complexity of [27] is medium, but it does not consider the impact of rotational speed on position errors. When $\omega_e = 0$, the phase shifts of the positive and negative sequence HF currents are completely offset, $\Delta\theta = 0$. When $\omega_e \neq 0$, the phase shifts of the positive and negative sequence HF currents are incompletely offset, $\Delta\theta = (\varphi_p^{sum} + \varphi_n^{sum})/2$, and the position error shows speed correlation.

Based on the above analysis, position error and computational complexity of the proposed method are the smallest. The proposed method reduces speed correlation.

5. EXPERIMENTAL VERIFICATION

To verify the correctness and feasibility of the proposed method, this paper uses RT-LAB to carry out hardware-in-the-loop (HIL) simulation experiments on the IPMSM drive system. The RT-LAB

Table 4. Main parameters and values of IPMSM.

Parameter	Value	Unit
Rated power	1.2	kW
Rated Speed	1500	rpm
Pole pairs	4	-
Stator resistance	2.8	Ω
d-axis inductance L_d	57	mH
q-axis inductance L_q	82	mH
Rated Torque	7.5	N · m
Moment of inertia J	0.003	Kg · m

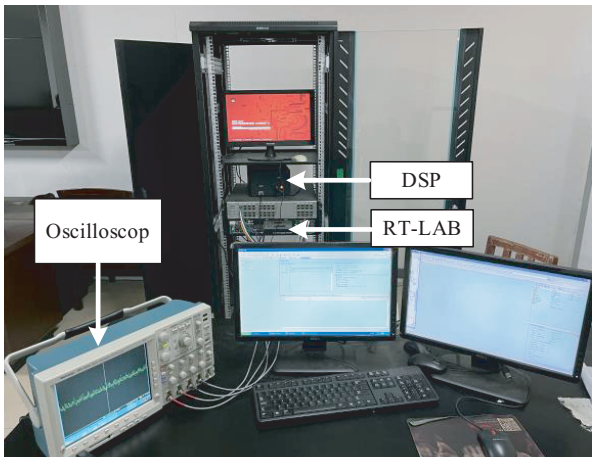

Figure 12. RT-LAB experimental platform.

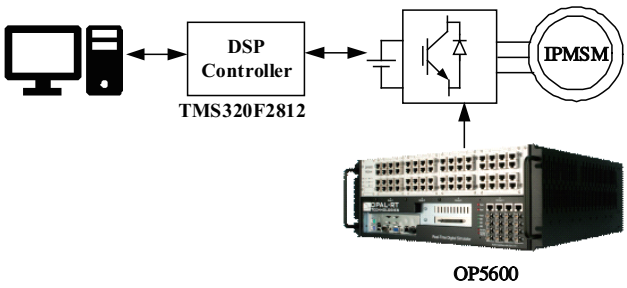

Figure 13. Schematic diagram of RT-LAB HILS.

experimental platform is shown in Fig. 12. Fig. 13 shows the RT-LAB in loop simulation diagram of IPMSM. The IPMSM parameters are shown in Table 4.

There are many literature studies on conventional methods for experimental comparison and analysis. In [23] and [25], the methods used are demodulation methods for estimating the d-q axis. However, the method proposed in [23] has greater computational complexity and a more complex demodulation process. Therefore, this paper has conducted experimental analysis and comparison with [25] and [27], which have simpler demodulation processes.

5.1. Experimental Results and Analysis of the Motor Running at 100 rpm without Load

When the motor runs at 100 rpm without load, the estimated and actual position, position error, and estimated and actual speed waveform are shown in Fig. 14, and $\Delta\theta$ comparison of the three methods is shown in Table 5. Compared with [27] and [25], the proposed method shows a 20% and 4.7% decrease in average position error.

The experimental results verify that the proposed method still has high position estimation accuracy after simplifying the current demodulation process.

5.2. Experimental Results and Analysis of Varying Speed

The no-load speed of the motor is 50 rpm. At 2 s, 5 s, 8 s, and 11 s, the speed rises to 100 rpm, 200 rpm, 300 rpm, and 400 rpm. The estimated and actual speed waveform and position error waveform are shown

Table 5. $\Delta\theta$ comparison of the three methods in experiment 5.1.

Method	$\Delta\theta_{\max}$/deg	*Range of* $\Delta\theta$/deg	$\Delta\theta_{avg}$/deg
Reference [27]	4.5	$4.5 \sim 0.5$	2.5
Reference [25]	4.2	$4.2 \sim 0$	2.1
Proposed method	4.0	$4.0 \sim -0.5$	2.0

Table 6. $\Delta\theta$ comparison of the three methods in experiment 5.2.

Method	$\Delta\theta_{\max}$/deg	*Range of* $\Delta\theta$/deg	$\Delta\theta_{avg}$/deg
Reference [27]	19.0	$19.0 \sim -0.5$	8.5
Reference [25]	8.0	$8.0 \sim -4.0$	4.0
Proposed method	8.0	$8.0 \sim -4.0$	4.0

in Fig. 15, and $\Delta\theta$ comparison of the three methods is shown in Table 6. The position error of [27] increases with the increase of rotational speed, while the position error of [25] and the proposed method changes less with the increase of rotational speed. Compared with [27], the proposed method has a 52.9% decrease in average position error. The method of [27] does not consider the effect of speed on position error. When the speed changes, the phase shift of positive and negative sequence HF currents also varies, resulting in a change in position error, thus exhibiting speed correlation.

The experimental results verify that the position error in [27] has speed correlation, and the proposed method simplifies the current demodulation process while eliminating the speed correlation of the position error.

5.3. Experimental Results and Analysis of Speedstep

The full load speed of the motor is 100 rpm. At 1 s, the speed gradually decreases from 100 rpm to -100 rpm, and at 5 s, the speed gradually increases from -100 rpm to 100 rpm. The A-phase current, estimated and actual speed, estimated and actual position, and position error waveform of this process are shown in Fig. 16, and $\Delta\theta$ comparison of the three methods is shown in Table 7. The estimation error in [27] declines with the decrease of speed and ultimately remains negative. Compared with [27], the proposed method shows a 31.0% decrease in the fluctuation range of position errors.

Table 7. $\Delta\theta$ comparison of the three methods in experiment 5.3.

Method	$\Delta\theta_{\max}$/deg	*Range of* $\Delta\theta$/deg	$\Delta\theta_{avg}$/deg
Reference [27]	6.0	$6.2 \sim -8.5$	4.2
Reference [25]	6.0	$6.0 \sim 6.0$	3.0
Proposed method	5.0	$5.0 \sim -5.0$	2.5

The experimental results also demonstrate that the proposed method simplifies the current demodulation process while eliminating speed correlation.

5.4. Experimental Results and Analysis of Full Load Step

The no-load speed of the motor is 100 rpm, and it starts to load to full load at 2 s and remains at full load for 8 s. At 11 s, motor starts to reduce load. The waveforms of A-phase current, current harmonic analysis, d-axis and q-axis current, estimated and actual speed, speed error and position error

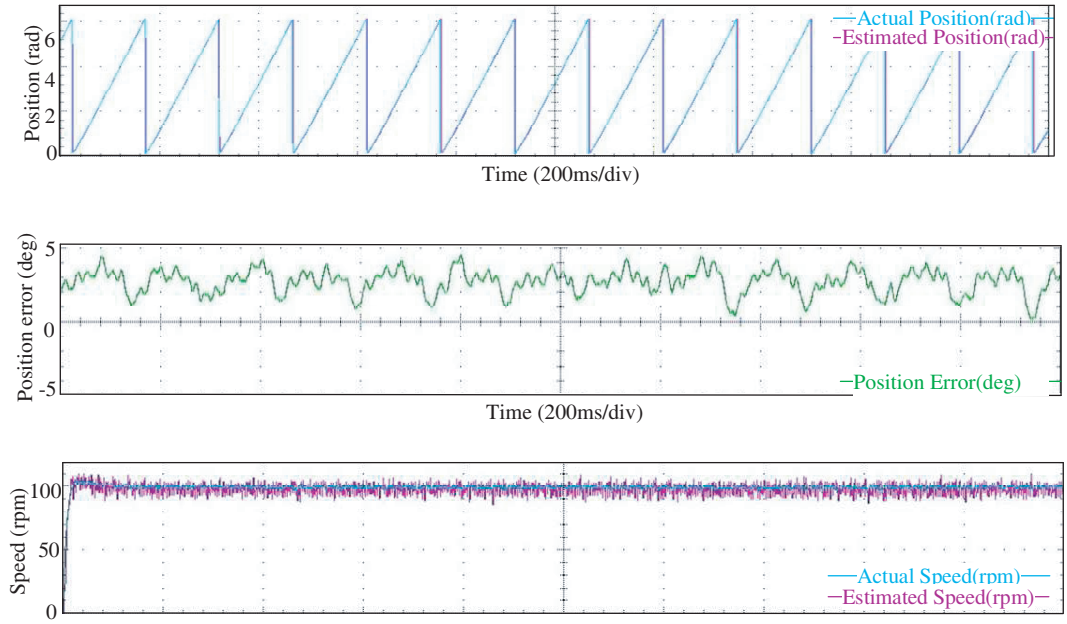
Actual Position(rad)
Estimated Position(rad)
Position (rad)
Time (200ms/div)
Position error (deg)
Position Error(deg)
Time (200ms/div)
Speed (rpm)
Actual Speed(rpm)
Estimated Speed(rpm)

(a)

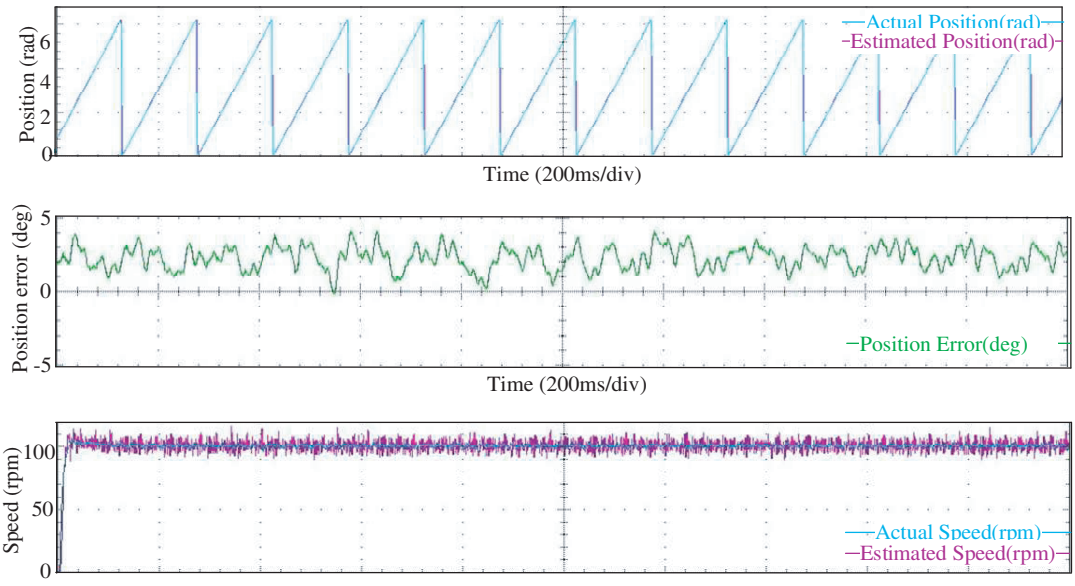
Actual Position(rad)
Estimated Position(rad)
Position (rad)
Time (200ms/div)
Position error (deg)
Position Error(deg)
Time (200ms/div)
Speed (rpm)
Actual Speed(rpm)
Estimated Speed(rpm)

(b)

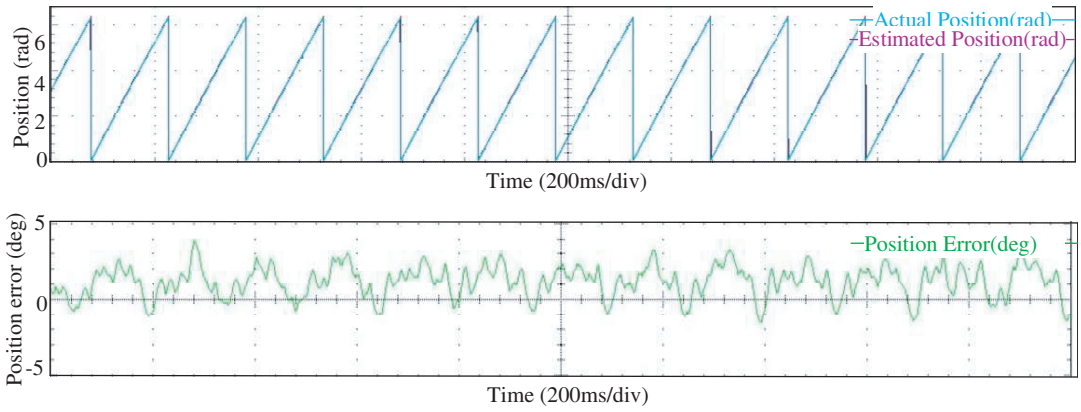
Actual Position(rad)
Estimated Position(rad)
Position (rad)
Time (200ms/div)
Position error (deg)
Position Error(deg)
Time (200ms/div)

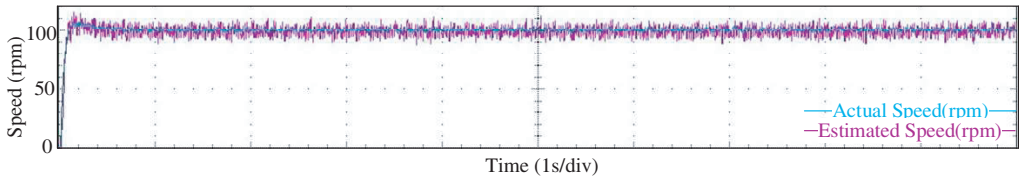

(c)

Figure 14. The estimated and actual positions, position errors, and estimated and actual speed waveforms of the motor running at 100 rpm without load. (a) Reference [27]. (b) Reference [25]. (c) Proposed method.

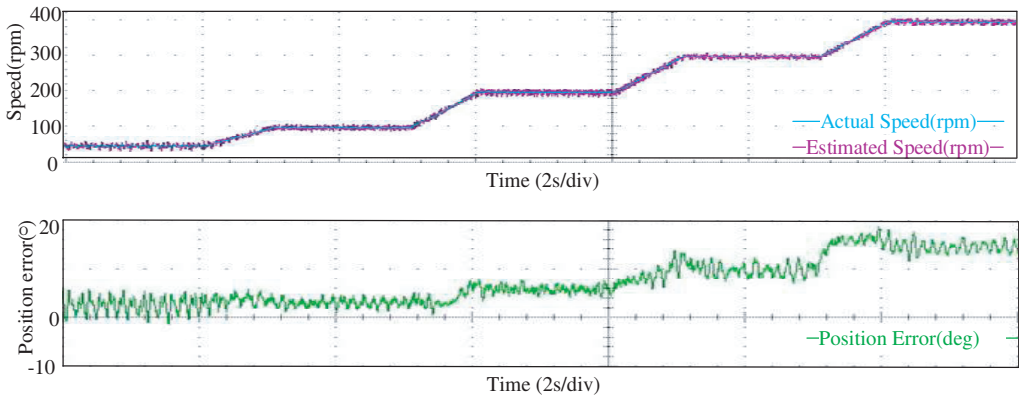

(a)

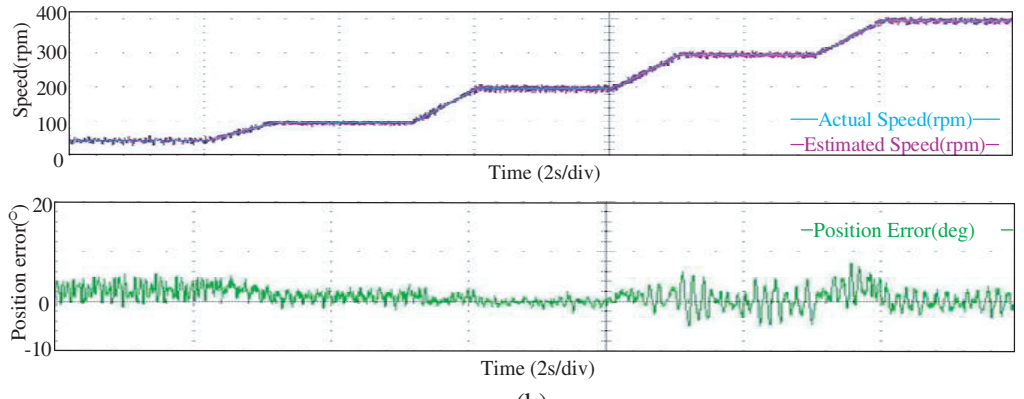

(b)

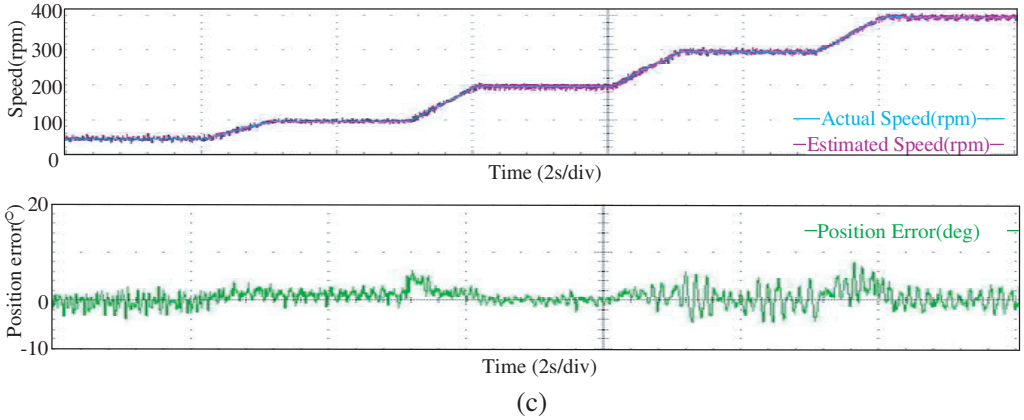

(c)

Figure 15. Theestimation and actual speed waveform and position error waveform of varying speed experiment. (a) Reference [27]. (b) Reference [25]. (c) Proposed method.

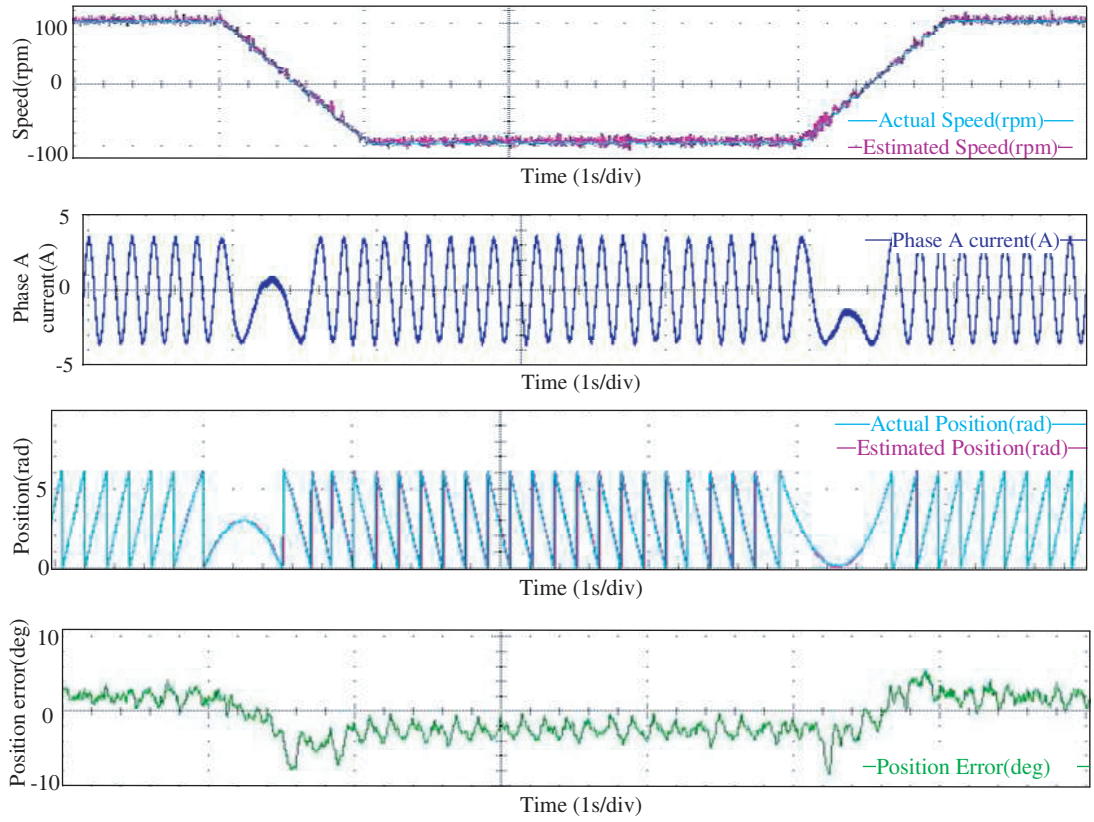
Speed(rpm)
100
0
-100
Actual Speed(rpm)
Estimated Speed(rpm)
Time (1s/div)
Phase A current(A)
5
0
-5
Phase A current(A)
Time (1s/div)
Position(rad)
5
0
Actual Position(rad)
Estimated Position(rad)
Time (1s/div)
Position error(deg)
10
0
-10
Position Error(deg)
Time (1s/div)

(a)

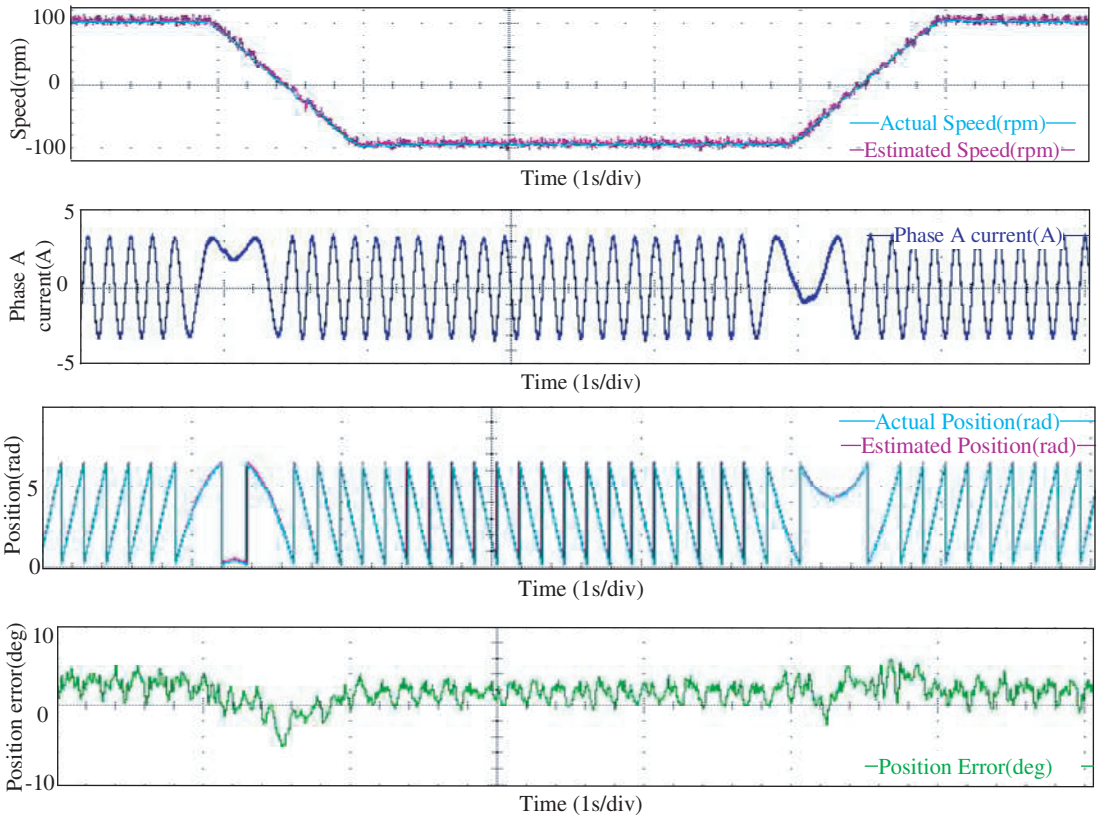
Speed(rpm)
100
0
-100
Actual Speed(rpm)
Estimated Speed(rpm)
Time (1s/div)
Phase A current(A)
5
0
-5
Phase A current(A)
Time (1s/div)
Position(rad)
5
0
Actual Position(rad)
Estimated Position(rad)
Time (1s/div)
Position error(deg)
10
0
-10
Position Error(deg)
Time (1s/div)

(b)

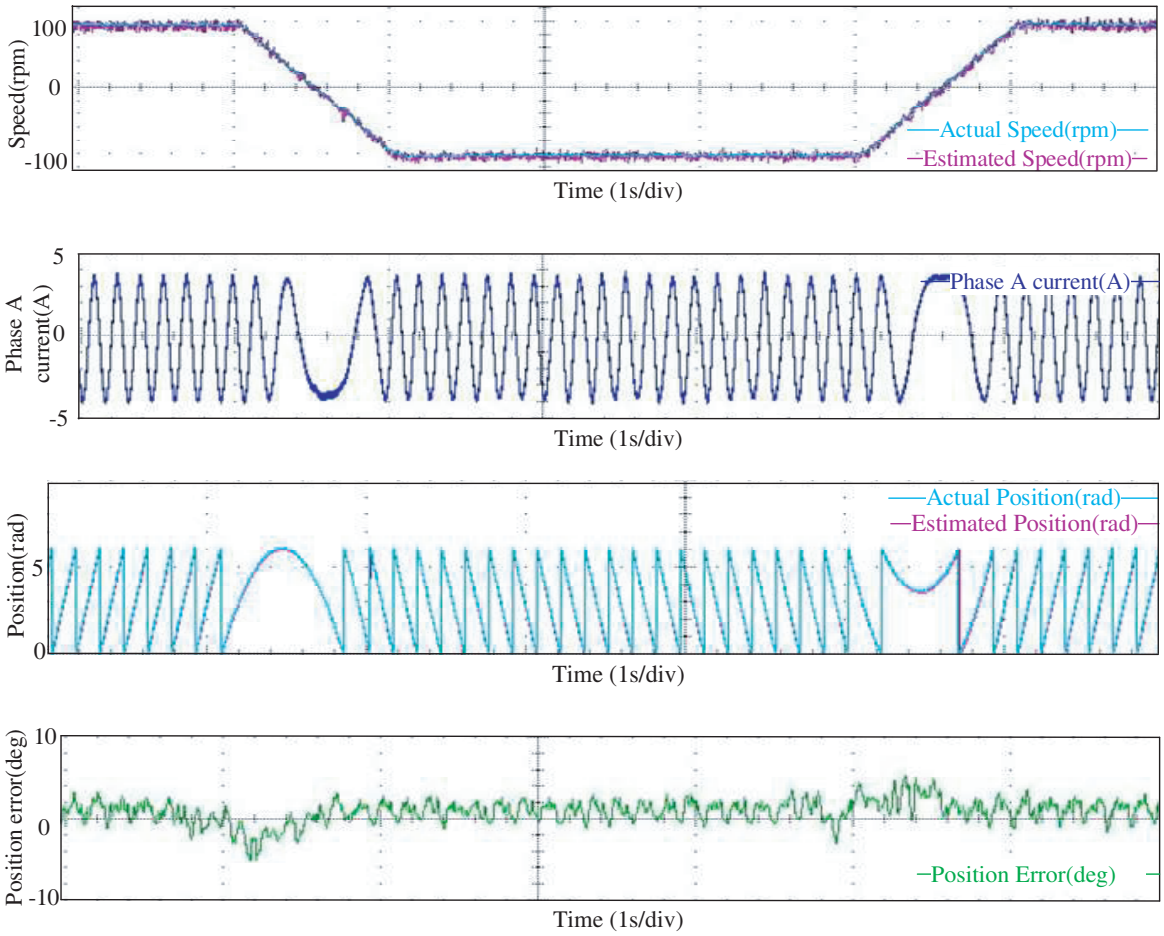

(c)

Figure 16. The estimation and actual speed, estimation and actual position, and position error waveform of speed step experiment. (a) Reference [27]. (b) Reference [25]. (c) Proposed method.

for loading and unloading are shown in Fig. 17, and $\Delta\theta$ and THD comparison of the three methods is shown in Table 8. The rotor position errors of the three methods fluctuate to a certain extent during loading and unloading. Compared with [27], the fluctuation range of position error decreases by 17.6%; the maximum value of velocity error decreases by 16.7%; and the harmonic distortion rate decreases by 3.0%.

The experimental results demonstrate that the proposed method shows good robustness to load disturbances after simplifying the current demodulation process.

Table 8. $\Delta\theta$ and THD comparison of the three methods in experiment 5.4.

Method	*Range of* $\Delta\theta$/deg	$\Delta\theta_{avg}$/deg	Δ*Speed*/rpm	*THD%*
Reference [27]	$10.0 \sim -7.0$	5.0	24	12.4
Reference [25]	$8.0 \sim -8.0$	4.0	22	10.5
Proposed method	$6.0 \sim 6$	3.0	20	9.2

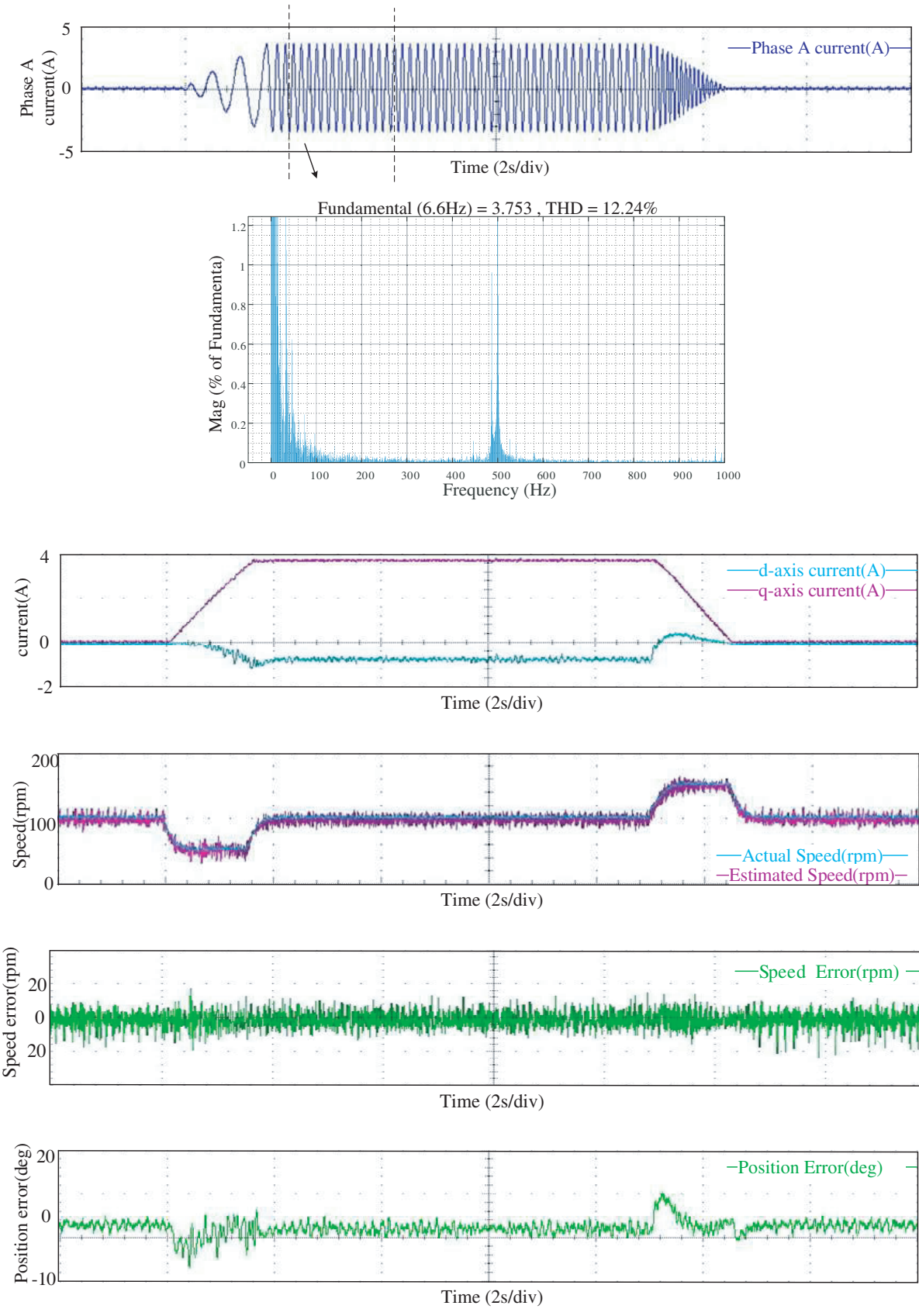
Phase A current(A)
Time (2s/div)
Fundamental (6.6Hz) = 3.753 , THD = 12.24%
Mag (% of Fundamenta)
Frequency (Hz)
d-axis current(A)
q-axis current(A)
current(A)
Time (2s/div)
Actual Speed(rpm)
Estimated Speed(rpm)
Speed(rpm)
Time (2s/div)
Speed Error(rpm)
Speed error(rpm)
Time (2s/div)
Position Error(deg)
Position error(deg)
Time (2s/div)

(a)

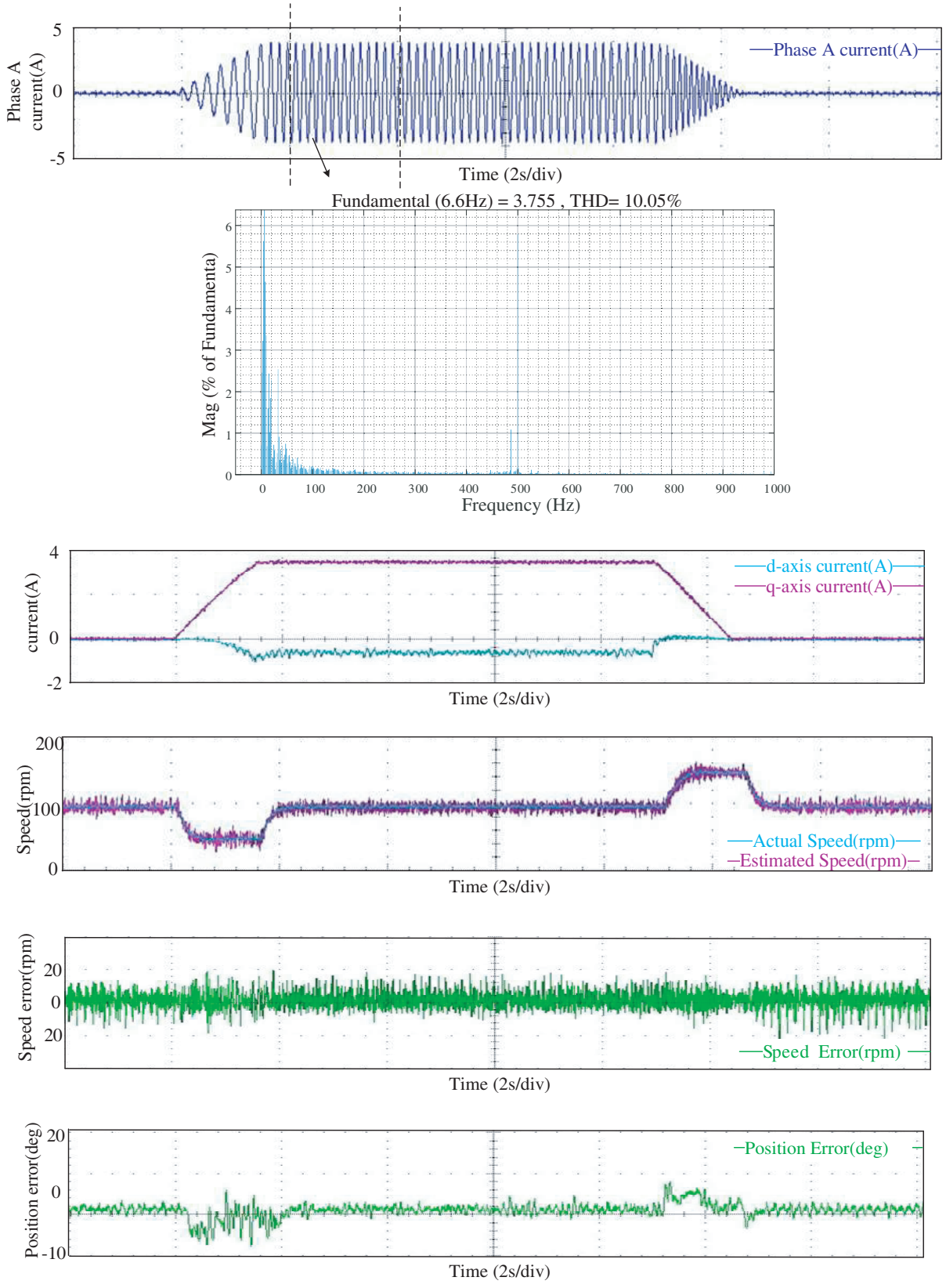
Phase A current(A)
Time (2s/div)
Fundamental (6.6Hz) = 3.755 , THD= 10.05%
Mag (% of Fundamenta)
Frequency (Hz)
d-axis current(A)
q-axis current(A)
current(A)
Time (2s/div)
Actual Speed(rpm)
Estimated Speed(rpm)
Speed(rpm)
Time (2s/div)
Speed Error(rpm)
Speed error(rpm)
Time (2s/div)
Position Error(deg)
Position error(deg)
Time (2s/div)

(b)

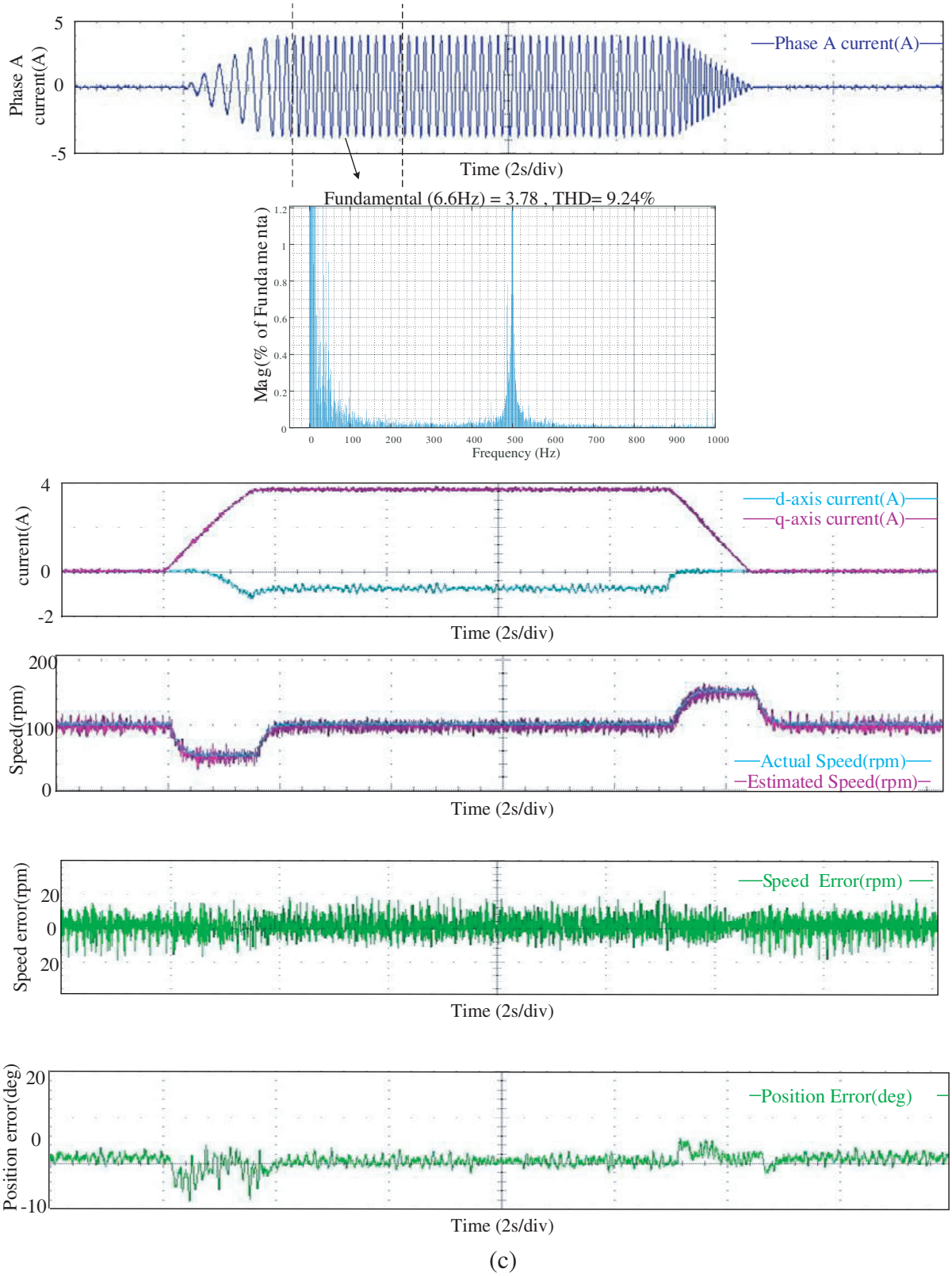

(c)

Figure 17. The A-phase current, *d*-axis and *q*-axis current, and position error waveform of full load step experiment. (a) Reference [27]. (b) Reference[25]. (c) Proposed method.

6. CONCLUSION

Based on simplifying the current demodulation process of the HRVI method, this paper proposes a sensorless control of IPMSM with TT current self-demodulation in the estimating d-q axis. Theoretical analysis and experimental results show:

(1) Compared with [25] and [27], the proposed method only requires one multiplication operation, does not require the use of demodulation signals, omits the process of separating positive and negative sequence currents, significantly simplifies the implementation process, and increases the practicality of the method.

(2) Compared with [27], the proposed method reduces the average position error value by 20.0% under steady-state conditions and the fluctuation range of position error under full load conditions by 17.6%. The position estimation accuracy is higher, and the robustness is better.

(3) Compared with [27], the proposed method reduces the average position error by 52.9% under variable speed conditions and the fluctuation range of position error under speed step conditions by 31.0%, and eliminates the influence of speed on position error.

ACKNOWLEDGMENT

This work was supported by the Natural Science Foundation of Hunan Province of China under Grant Number 2022JJ50094.

REFERENCES

1. Junejo, A. K., W. Xu, C. Mu, et al., "Adaptive speed control of PMSM drive system based a new sliding-mode reaching law," *IEEE Transactions on Power Electronics*, Vol. 35, No. 11, 12110–12121, 2020.
2. Woldegiorgis, A. T., X. Ge, S. Li, et al., "An improved sensorless control of IPMSM based on pulsating high-frequency signal injection with less filtering for rail transit applications," *IEEE Transactions on Vehicular Technology*, Vol. 70, No. 6, 5605–5617, 2021.
3. Wang, S., Z. Li, D. Wu, et al., "Sensorless control of SPMSM based on high-frequency positive- and negative-sequence current dual-demodulation," *IEEE Transactions on Industrial Electronics*, Vol. 70, No. 5, 4631–4639, 2022.
4. Wu, C., Z. Chen, and Q. Chen, "Hybrid-modulation-based full-speed sensorless control for permanent magnet synchronous motors," *IEEE Transactions on Power Electronics*, Vol. 37, No. 5, 5908–5917, 2021.
5. Zhang, Y., Z. Yin, X. Cao, et al., "A novel SPMSM sensorless drive using discrete-time synchronous-frequency adaptive observer under low frequency ratio," *IEEE Transactions on Power Electronics*, Vol. 37, No. 9, 11045–11057, 2022.
6. Mai, Z., F. Xiao, K. Fu, et al., "HF pulsating carrier voltage injection method based on improved position error signal extraction strategy for PMSM position sensorless control," *IEEE Transactions on Power Electronics*, Vol. 36, No. 8, 9348–9360, 2021.
7. Dong, S., M. Zhou, X. You, et al., "A sensorless control strategy of injecting HF voltage into d-axis for IPMSM in full speed range," *IEEE Transactions on Power Electronics*, Vol. 37, No. 11, 13587–13597, 2022.
8. Li, H., X. Zhang, C. Xu, et al., "Sensorless control of IPMSM using moving-average-filter based PLL on HF pulsating signal injection method," *IEEE Transactions on Energy Conversion*, Vol. 35, No. 1, 43–52, 2019.
9. Chen, D., J. Wang, and L. Zhou, "Adaptive second-order active-flux observer for sensorless control of PMSMs with MRAS-based VSI non-linearity compensation," *IEEE Journal of Emerging and Selected Topics in Power Electronics*, Vol. 11, No. 3, 3076–3086, 2023.

10. Xu, Y., C. Wang, W. Yuan, et al., "Anti-disturbance position sensorless control of PMSM based on improved sliding mode observer with suppressed chattering and no phase delay," *Journal of Electrical Engineering & Technology*, 1–13, 2023.
11. Darani, A. Y. and B. M. Dehkordi, "Sensorless control of a surface-mounted PMSM by an improved flux observer with RLS parameter identification method," *IEEE Power Electronics, Drive Systems, and Technologies Conference*, 1–7, 2023.
12. Naderian, M., G. A. Markadeh, M. Karimi-Ghartemani, et al., "Improved sensorless control strategy for IPMSM using an ePLL approach with high-frequency injection," *IEEE Transactions on Industrial Electronics*, Vol. 71, No. 3, 2231–2241, 2023.
13. Mai, Z., F. Xiao, K. Fu, et al., "HF pulsating carrier voltage injection method based on improved position error signal extraction strategy for PMSM position sensorless control," *IEEE Transactions on Power Electronics*, Vol. 36, No. 8, 9348–9360, 2021.
14. Lin, Z., X. Li, Z. Wang, et al., "Minimization of additional high-frequency torque ripple for square-wave voltage injection IPMSM sensorless drives," *IEEE Transactions on Power Electronics*, Vol. 35, No. 12, 13345–13355, 2020.
15. Zhang, X., H. Li, S. Yang, et al., "Improved initial rotor position estimation for PMSM drives based on HF pulsating voltage signal injection," *IEEE Transactions on Industrial Electronics*, Vol. 65, No. 6, 4702–4713, 2017.
16. Xu, P. and Z. Zhu, "Carrier signal injectionbased sensorless control for permanent magnet synchronous machine drives with tolerance of signal processing delays," *IET Electric Power Applications*, Vol. 11, No. 6, 1140–1149, 2017.
17. Li, C., G. Wang, G. Zhang, et al., "Adaptive pseudorandom high-frequency square-wave voltage injection based sensorless control for SynRM drives," *IEEE Transactions on Power Electronics*, Vol. 36, No. 3, 3200–3210, 2020.
18. Du, S., Quanli, and X. Zhu, "Fault tolerant control of position sensor failure in permanent magnet synchronous motors at zero and low speeds based on high-frequency injection," *Chinese Journal of Electrical Engineering*, Vol. 39, No. 10, 3038–3046, 2019.
19. Sun, X., T. Li, Z. Zhu, et al., "Speed sensorless model predictive current control based on finite position set for PMSHM drives," *IEEE Transactions on Transportation Electrification*, Vol. 7, No. 3, 2743–2752, 2021.
20. Sun, X., T. Li, M. Yao, et al., "Improved finite-control-set model predictive control with virtual vectors for PMSHM drives," *IEEE Transactions on Energy Conversion*, Vol. 37, No. 3, 1885–1894, 2021.
21. Yang, J., S. Yang, H. Li, et al., "Analysis and compensation of the error in initial rotor position of IPMSM estimated with HF signal injection," *IEEE Transportation Electrification Conference and Expo*, 1–5, 2017.
22. Li, H., X. Zhang, S. Yang, et al., "Improved initial rotor position estimation of IPMSM using amplitude demodulation method based on HF carrier signal injection," *Annual Conference of the IEEE Industrial Electronics Society*, 1996–2001, 2017.
23. Liu, S., S. Yang, H. Li, et al., "Position observation of built-in permanent magnet synchronous motor using rotational high-frequency injection method based on rotational coordinate system demodulation," *Journal of Electrical Engineering Technology*, Vol. 35, No. 4, 708–716, 2020.
24. Mai, Z., F. Xiao, J. Liu, W. Zhang, and C. Lian, "Rotating high-frequency voltage injection method based on improved self adjusting shaft amplitude convergence current demodulation method," *Journal of Electrical Engineering*, Vol. 36, No. 10, 2049–2060, 2021.
25. Mai, Z., J. Liu, F. Xiao, K. Li, and Y. Zheng, "An improved high-frequency rotating voltage injection sensorless control strategy based on estimated position feedback current demodulation method," *Journal of Electrical Engineering*, Vol. 37, No. 4, 870-881+891, 2022.
26. Wang, G., D. Xiao, G. Zhang, et al.,"Sensorless control scheme of IPMSMs using HF orthogonal square-wave voltage injection into a stationary reference frame," *IEEE Transactions on Power Electronics*, Vol. 34, No. 3, 2573–2584, 2018.

27. Li, W., J. Liu, J. Gao, et al., "High frequency response current self-demodulation method for sensorless control of interior permanent magnet synchronous motor," *IEEE Access*, Vol. 9, 157093–157105, 2021.
28. Yu, X., "Sensorless control technology for permanent magnet synchronous motors in the full speed range," Hunan University of Technology, 2022.
29. Liu, J., K. Fu, Z. Mai, et al., "An improved high-frequency pulse voltage injection sensorless control strategy based on dual frequency notch filter," *Chinese Journal of Electrical Engineering*, Vol. 41, No. 2, 749–759, 2021.